



Impact of IrRu oxygen evolution reaction catalysts on Pt nanostructured thin films under start-up/shutdown cycling

David A. Cullen^{a,*}, Karren L. More^b, Ljiljana L. Atanasoska^c, Radoslav T. Atanasoski^c

^a Materials Science & Technology Division, Oak Ridge National Laboratory, Oak Ridge, TN 37831, USA

^b Center for Nanophase Materials Sciences, Oak Ridge National Laboratory, Oak Ridge, TN 37831, USA

^c 3M Company Fuel Cell Components Program, St. Paul, MN 55144, USA

HIGHLIGHTS

- Ultralow loadings of Ir and Ru were deposited on Pt nanostructured thin films.
- The IrRu catalysts promote the oxygen evolution reaction during fuel cell tests.
- Catalyst morphology was studied before and after start-up/shutdown tests.
- Morphological changes were correlated with catalyst loading and activity.
- Dissolved Pt, Ir, and Ru were found in the membrane and microporous layer.

ARTICLE INFO

Article history:

Received 22 April 2014

Received in revised form

17 June 2014

Accepted 27 June 2014

Available online 12 July 2014

Keywords:

Fuel cells

Start-up/shutdown

Oxygen evolution reaction

Catalyst

Scanning transmission electron microscopy

X-ray photoelectron spectroscopy

ABSTRACT

Electron microscopy and X-ray photoelectron spectroscopy (XPS) were utilized to study the role of oxygen evolution reaction (OER) catalysts in mitigating degradation arising from start-up/shutdown events. Pt nanostructured thin films (NSTF) were coated with a $\text{Ru}_{0.1}\text{Ir}_{0.9}$ OER catalyst at loadings ranging from 1 to $10 \mu\text{g cm}^{-2}$ and submitted to 5000 potential cycles within a membrane electrode assembly. Analysis of the as-deposited catalyst showed that the Ir and Ru coating is primarily metallic, and further evidence is provided to support the previously reported interaction between Ru and the perylene-red support. Aberration-corrected scanning transmission electron microscopy and energy dispersive X-ray spectroscopy were used to observe the impact of the OER catalysts on Pt dissolution and migration into the membrane. Elemental mapping showed a high percentage of the Ir catalyst was maintained on the NSTF whisker surfaces following testing. The presence of the OER catalysts greatly reduced the smoothing of the Pt NSTF whiskers, which has been correlated with Pt dissolution and losses in electrochemically active surface area. The dissolution of both Ir and Pt led to the formation of IrPt nanoparticle clusters in the membrane close to the cathode, as well as the formation of a Pt band deeper in the membrane.

Published by Elsevier B.V.

1. Introduction

Polymer electrolyte membrane fuel cells (PEMFCs) are under intense research and development for transportation applications. Vehicles powered by hydrogen fuel cells would provide a driving experience comparable to today's gas powered vehicles, while producing only water and heat as by-products [1]. However, the durability of the fuel cell electrodes is severely impacted by frequent start-up/shutdown (SU/SD) events that occur during normal vehicle use, which has garnered much attention from the

PEMFC community over the past several years [2,3]. During SU/SD, a reverse-current condition occurs in the section of the fuel cell where air is present at both the anode and the cathode, with carbon corrosion and oxygen evolution reactions taking place at the cathode and oxygen reduction at the anode. The resulting spike in the cathode potential leads to rapid corrosion of the carbon support and agglomeration, encapsulation, and dissolution of the Pt oxygen reduction reaction (ORR) nanoparticle catalyst. Such degradation causes a steady decay in fuel cell performance and can ultimately lead to stack failure.

While several systems-based strategies have been employed to mitigate the effects of SU/SD on fuel cell durability, a materials-based strategy is preferred. Most materials-based approaches have focused on developing corrosion resistant supports [3,4]. An

* Corresponding author.

E-mail address: cullenda@ornl.gov (D.A. Cullen).

alternate strategy involves the incorporation of catalysts that favor the oxygen evolution reaction (OER), thus lowering the overall electrode potential and reducing Pt dissolution and carbon corrosion [5]. According to Trasatti, the two most active OER catalysts are the oxides of ruthenium and iridium [6]. While ruthenium oxide is among the most active OER materials, it must be stabilized in the acidic PEMFC environment. Iridium also has a high OER activity, with the added benefit of acting as a stabilizer for ruthenium [7].

In this work, different loadings of ruthenium and iridium have been incorporated onto 3M's unique Pt nanostructured thin film (NSTF) catalyst. The NSTF support consists of a dense, oriented array of organic perylene-red "whiskers", which are subsequently coated with Pt through a vacuum deposition process that forms a continuous, thin, film-like layer over the NSTF whiskers, consisting of highly oriented, individual Pt grains ranging from 5 to 15 nm in size [8,9]. The end product is a corrosion-resistant support with a stable catalyst, which is less susceptible to dissolution or agglomeration than its carbon-supported nanoparticle counterpart.

It was previously demonstrated that the addition of even minute amounts of IrRu catalysts to the Pt NSTF leads to a marked improvement in the robustness of the fuel cell to SU/SD conditions by facilitating water electrolysis at reduced potentials compared to that of pure Pt NSTF electrodes [10]. The present work aimed at evaluating changes to the Pt and OER catalysts at the nm-scale, providing insight into degradation mechanisms, such as catalyst coalescence, dissolution, and alloying, and guidance for improving the activity and stability of these high-cost materials. Here, various electron microscopy techniques, including scanning electron microscopy (SEM), aberration-corrected scanning transmission electron microscopy (STEM), and energy dispersive X-ray spectroscopy (EDS), were employed to study the morphology and compositional changes of the OER and ORR catalysts before and after testing. The OER catalyst and the interfaces generated by its deposition were characterized by X-ray photoelectron spectroscopy (XPS). These methods can provide valuable information on the durability and behavior of the OER catalysts under SU/SD conditions, the interaction of the OER catalysts with the NSTF-supported Pt, and the impact of OER loading on Pt dissolution.

2. Experimental

Details on the growth of the perylene-red NSTF substrate and subsequent coating with Pt metal have been described elsewhere [8]. For the present experiments, a low Pt loading of $85 \mu\text{g cm}^{-2}$ was used for all the samples. Ru and Ir metal were deposited on the whisker surfaces by physical vapor deposition (PVD) at loadings of 1, 2, 5, and $10 \mu\text{g cm}^{-2}$; the atomic ratio of Ru to Ir was 1:9 for all cases. For a justification of this particular formulation, see Ref. [5]. The elemental composition of these samples, derived from the low resolution XPS survey spectra was reported previously [10]. The surface chemical states of Ir, Ru, and Pt in the NSTF samples were determined in this study from the XPS core level spectra. The details on the XPS data acquisition and curve fitting analysis parameters for Ir 4f and C 1s–Ru 3d core level spectra have already been described [5]. The curve fitting analysis of Pt 4f core level spectra was done by constraining the branching ratio and binding energy (BE) splitting of Pt $4f_{7/2}$ –Pt $4f_{5/2}$ spin orbital doublet at their theoretical values 4:3 and 3.33 eV, respectively.

The NSTF was transferred into catalyst-coated membranes (CCMs) via the roll-good process [8]. A Pt NSTF electrode decorated with the $\text{Ru}_{0.1}\text{Ir}_{0.9}$ catalyst was used as the cathode, with a bare Pt NSTF electrode at the anode. The electrodes were separated by a 50 μm membrane (3M PEM 825 eq. weight). Membrane electrode assemblies (MEA) were prepared by placing the CCM between two gas diffusion layers (GDL) with a microporous layer (MPL).

The specific details of the SU/SD testing protocol and electrochemical measurements have been previously published [10]. The protocol consisted of 5000 triangular-wave potential cycles, which used a combined charge/voltage limit. The potential was ramped upward from 0.9 V until either the potential (1.6 V) or charge (5 mC cm^{-2}) limit was reached.

In preparation for STEM imaging, MEAs were disassembled and stripped of the GDL layer, then mounted in epoxy, and subsequently sectioned by diamond-knife ultramicrotomy [11]. Cross-sectional MEAs with a nominal thickness of 50–75 nm were mounted on Cu grids for observation and EDS mapping in a JEOL 2200FS aberration-corrected STEM equipped with a Bruker XFlash silicon drift detector. The trimmed microtome blocks were mounted on Al stubs such that the freshly cut MEA surfaces could be imaged in a JEOL 6500F SEM.

3. Results and discussion

3.1. Nature of IrRu overlayer

In order to understand the impact of SU/SD events on the Pt and OER catalysts, the nature of the NSTF overlayers was first thoroughly characterized by STEM and XPS. Fig. 1 shows a low magnification bright-field (BF) STEM image of a pristine NSTF cathode, along with higher magnification images of a single whisker. The coarse appearance of the whisker surface arises from the structured nature of the Pt film, which is made up of individual columnar Pt grains with an average size on the order of 10 nm. The bare-Pt and OER catalyst-coated Pt-NSTF surfaces, Fig. 1c and d, respectively, appear very similar, indicating that the IrRu catalyst grows epitaxially on the surface of Pt grains. Pt and Ir have the same face-centered-cubic crystal structure and very similar lattice parameters, and thus epitaxial growth would be expected. Due to the epitaxial growth of Ir on Pt, their similarity in atomic number, and the thinness of the Ru layer, the different elements cannot readily be distinguished by using either BF-STEM or high angle annular dark field (HAADF) STEM imaging. Thus, it is not possible to discern the coverage and uniformity of the OER catalyst layer on the Pt-NSTF surfaces directly by imaging. A non-continuous OER catalyst layer would be preferred over a continuous film, as complete coverage of the Pt-NSTF surfaces would block the Pt catalyst ORR sites, thus negatively impacting fuel cell performance. However, the loadings used in this study are so low that a fully continuous coating of the Pt is unlikely. Even for the highest OER loading, an even coating over the Pt-NSTF would result in layer thicknesses of only 1 nm of Ir and a single monolayer of Ru.

Previous XPS results for the 2 and $10 \mu\text{g cm}^{-2}$ IrRu catalyst layers deposited over the thick 0.15 mg cm^{-2} Pt film showed that Ir and Ru are mostly metallic [5]. Here, the contribution of Ir and Ru metallic form in the epitaxial IrRu layers grown in a systematic manner over a significantly thinner Pt film of $85 \mu\text{g cm}^{-2}$ is examined. We reported earlier the observed trend in the change of Ir, Ru, Pt, and C atomic concentration at the evolving IrRu–Pt–NSTF interface, specifically that the increase in Ir is matched by a decline in Pt, while the increase in Ru mirrors that of the declining perylene-red carbon [10]. For completeness of the elemental composition evaluation, especially for a reliable assessment of the contribution of Ir and Ru metallic forms, we expand that analysis here to include oxygen concentration profiles (Fig. 2). This figure shows that the O growth profile is noticeably slower than that of Ir; the O content increases from ~10 to ~25% atomic as growth of the OER catalyst proceeds.

The catalyst oxidation states and contributions of Ir, Ru, and Pt metallic form at the interface are determined from the high resolution XPS core level spectra. The change in the core level spectra and the representative curve-fitting analysis of core level peaks are

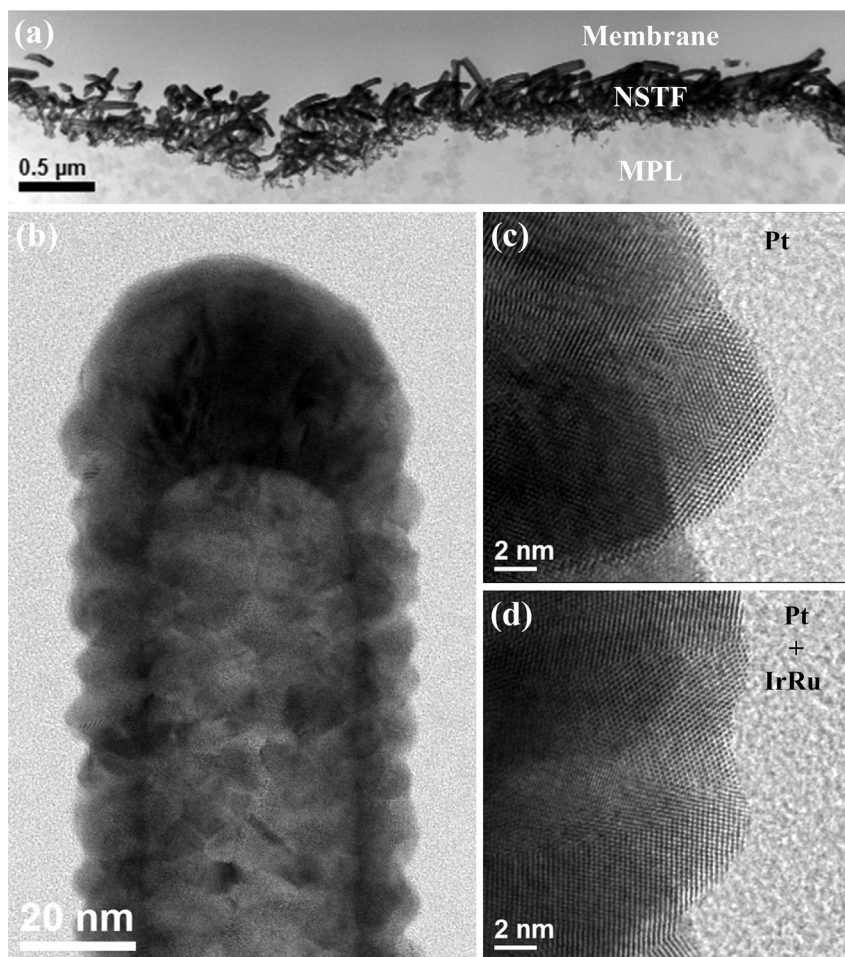


Fig. 1. Bright-field STEM images of (a) Pt-NSTF cathode layer, (b) individual Pt-NSTF whisker and whisker surfaces (c) without and (d) with IrRu OER catalyst. In this formulation, the OER catalyst grows epitaxially on the surfaces of the Pt grains.

presented in Figs. 3–5. The Ir 4f and Pt 4f core level peaks, plotted together in Fig. 3(a) for different OER catalyst loadings, clearly illustrate that the attenuation of platinum is mirrored by an increase in Ir. The actual change in the Ir and Pt surface atomic concentrations, quantified from the low resolution XPS survey spectra,

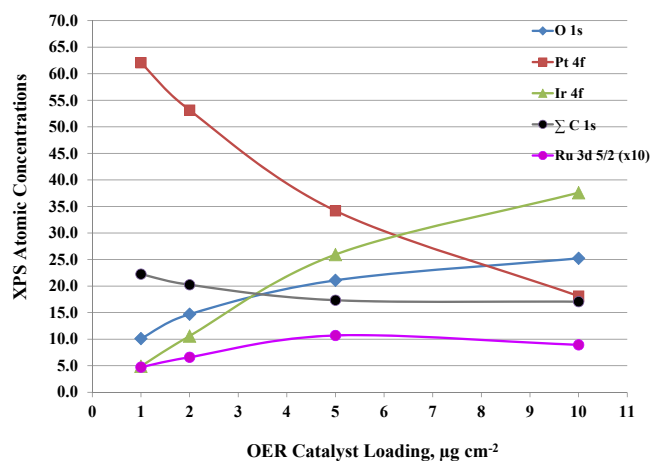


Fig. 2. Atomic concentration profiles derived from XPS survey spectra for varying IrRu loadings on Pt-coated NSTF.

can be extracted from Fig. 2. The binding energy locations and the line-shapes of Ir 4f and Pt 4f core level doublets in Fig. 3(a) indicate that both Ir and Pt are predominantly metallic for all four OER catalyst loadings. As seen from the high resolution C 1s – Ru 3d core level spectra in Fig. 3(b), the Ru 3d_{5/2} peak intensity does not seem to change much with the rising OER catalyst loadings. This is in agreement with the quantitative surface analysis in Fig. 2, which demonstrates that the growth in Ru content is visibly slower than that of Ir.

The curve fitting analysis of the raw core level data was done in order to resolve and quantify the contribution of multiple chemical states of Ir, Pt, Ru, C, and O, especially to determine the contribution of metallic form of Ir, Pt and Ru within the epitaxial interface. The atomic concentrations of the resolved metallic and reacted Ir, Ru and Pt derived from the XPS data are compiled in Table 1.

Three different Ir chemical states were resolved by the curve fitting analysis; as seen from Fig. 4a,b, the Ir 4f line shape can be fitted with three resolved Ir 4f_{7/2-5/2} doublets. The first, most intense Ir 4f_{7/2} peak at ~60.9 eV, corresponds to Ir metallic state. The second, considerably weaker Ir 4f_{7/2} peak at ~61.5 eV, shifted by ~0.6 eV relative to un-reacted metallic iridium peak, is associated with the oxidized Ir (III) and (IV) states [10,12]. The photo-emission of the third resolved iridium peak at ~63 eV is most probably related to the final state screening phenomena, associated with various forms of iridium oxide, and thus considered as a contribution of reacted iridium [13].

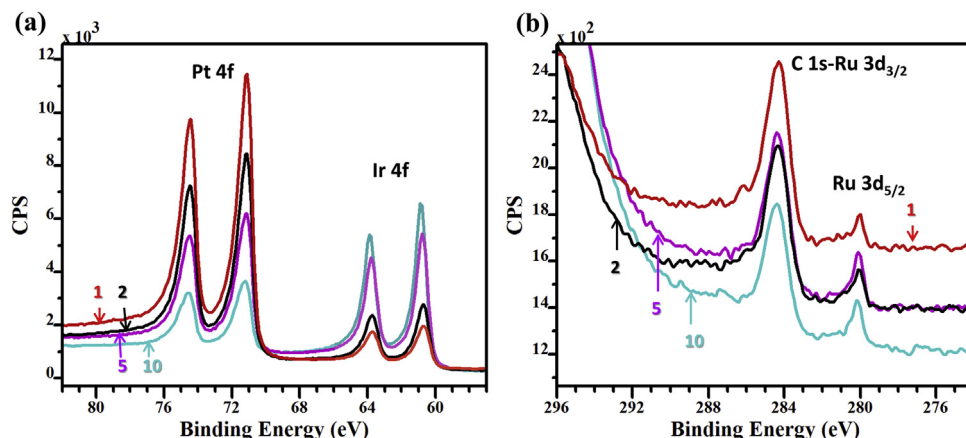


Fig. 3. (a) Pt 4f, Ir 4f and (b) C 1s-Ru 3d core levels XPS spectra for varying IrRu loadings on Pt-coated NSTF.

As seen from Table 1 and Fig. 2, the contribution of metallic Ir is prevailing; about 80% of the total content is present in metallic form for all investigated OER catalyst loadings. This high level of metallic Ir present at the interface correlates well with the observed epitaxial growth on Pt in STEM images.

The Pt 4f core level line shape can also be fitted with three resolved Pt 4f_{7/2}-5/2 doublets, indicating three different platinum chemical states (Fig. 4c,d). The most intense Pt 4f_{7/2} peak at ~71.2 eV is associated with Pt metallic state. The low intensity Pt 4f_{7/2} peak at ~72.0 eV, shifted by ~0.8 eV relative to un-reacted metallic platinum peak, corresponds to platinum (II) oxide states such as PtO or Pt₂O [14]. The third resolved platinum peak at ~73 eV is most probably related to Pt(IV) oxides. As in the case of iridium, the third resolved Pt peak could also contain contributions of the final state screening.

The contribution of metallic Pt form is at the constant high level of about 70% of the overall Pt content for all IrRu loadings (Table 1, Fig. 2). The slightly higher level of oxidized/ reacted Pt, when compared to iridium, could be rationalized by a higher probability for Pt to interact with perylene-red, due to their direct interface contact. The predominant presence of metallic Ir and metallic Pt at the interface correlates well with the observed epitaxial growth behavior.

Fig. 5a,b shows the curve fitting analysis of C 1s-Ru 3d core levels spectra for 2 and 10 $\mu\text{g cm}^{-2}$ OER catalyst loadings. The C 1s-Ru 3d core level spectra are complex because the perylene red aliphatic and aromatic carbon peak overlaps with the Ru 3d_{3/2} photoemission. Only the perylene-red carbonyl carbon peak appears as a distinctive feature at binding energy of ~288 eV. However, in spite of the C 1s-Ru 3d line-shape complexity, even without

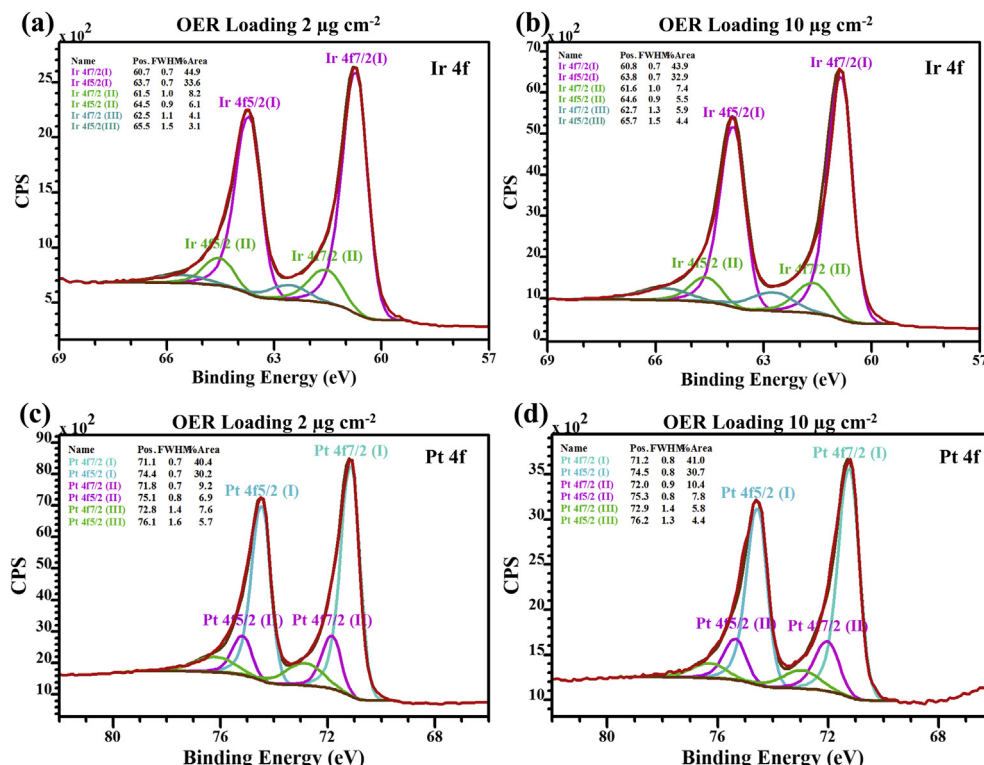


Fig. 4. Curve fitting analysis of (a,b) Ir 4f and (c,d) Pt 4f core level spectra for OER catalyst loadings of 2 $\mu\text{g cm}^{-2}$ and 10 $\mu\text{g cm}^{-2}$.

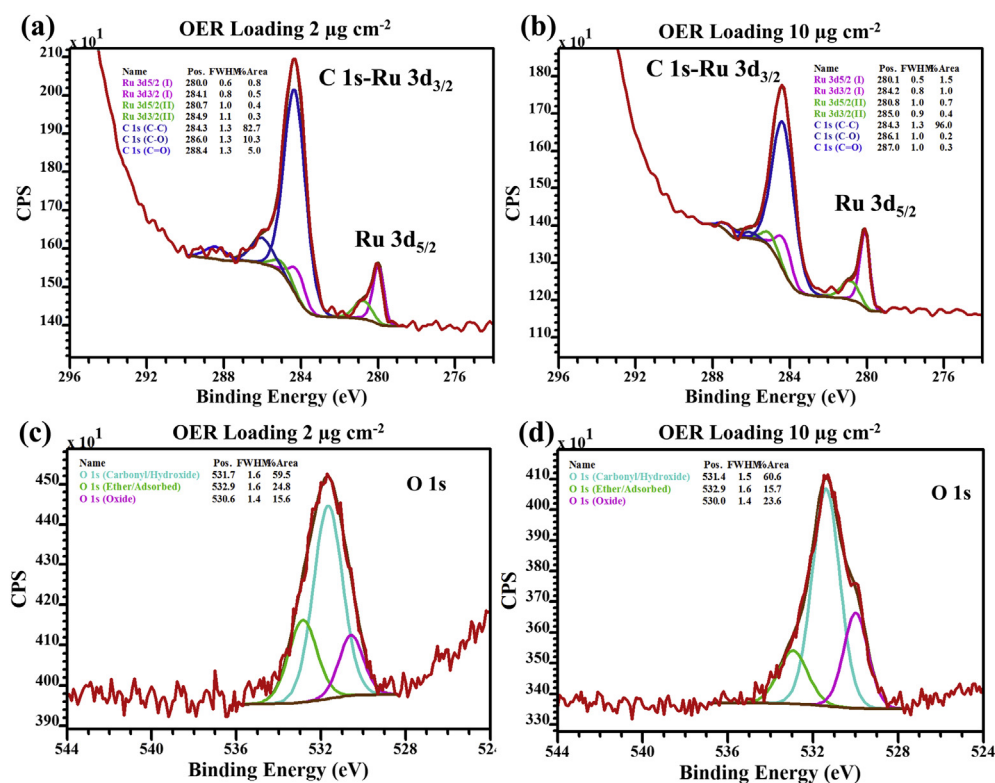


Fig. 5. Curve fitting analysis of (a,b) C 1s-Ru 3d and (c,d) O 1s core level spectra for OER catalyst loadings of $2 \mu\text{g cm}^{-2}$ and $10 \mu\text{g cm}^{-2}$.

resolving the overlapped peaks by curve fitting, the actual line-shape of Ru $3d_{5/2}$ photoemission indicates the existence of multiple Ru chemical states. The main Ru $3d_{5/2}$ peak, which appears at BE location of 280.0 eV is characteristic of metallic Ru. A notable Ru $3d_{5/2}$ peak shoulder at BE of ~ 280.8 eV, shifted by ~ 0.8 eV with respect to the metallic BE location, indicates the presence of reacted Ru. The contribution of reacted Ru state does not change with OER loadings; it is $\sim 30\%$ of the total Ru content (Table 1, Fig. 2).

The curve fitting analysis of C 1s – Ru 3d core level spectra provides additional evidence that the interactions occur at the IrRu-Pt-NSTF interface. Besides the resolved reacted Ru surface states, the presence of a carbon peak at 287 eV is also revealed. This carbon peak is associated with the ether like C–O single bonds. Our previous studies of the interfaces, formed by depositing Ru and Ir overlayers separately onto the perylene-red whiskers, show that the ether carbon peak emerges after Ru or Ir deposition as a result of their interaction with the perylene-red carbonyl groups; the ether carbon peak is absent in the case of clean perylene-red. When compared to Ir, the extent of Ru interaction with the perylene-red carbonyl groups was significantly more pronounced [12]. Thus, in this case it is most likely that the perylene-red carbonyl groups

primarily interact with the adjacent layer of Pt and with the Ru, which landed at the exposed perylene-red sites.

The interpretation of the O 1s core level spectra is challenging, because it contains contributions not only from the oxidized portions of Ir, Pt, and Ru but also from the perylene-red carbonyl groups; there are overlapped peaks that cannot be resolved by curve fitting. Fig. 5c,d shows the curve fitting analysis of O 1s core levels spectra for 2 and $10 \mu\text{g cm}^{-2}$ OER catalyst loadings with the three resolved oxygen peaks. The oxygen peak at ~ 531.5 eV is the most intense for all IrRu loadings. The 531.5 eV oxygen peak contains the overlapping photoemission from the carbonyl oxygen and metal oxygen sigma bonds found in compounds such as PtO , Ir_2O_3 or RuO_x . The oxygen peak at ~ 530 eV is associated with the oxide oxygen (or metal oxygen π bonds present in compounds such as PtO_2 , IrO_2 and RuO_2) [15]. As seen from Fig. 5a,b, the oxide oxygen peak slightly increases with the IrRu loadings. The third resolved oxygen peak at BE of ~ 533 eV corresponds to ether type oxygen. The emergence of ether oxygen peak related to the metallo-organic bonds formed by Ru and Ir interaction with perylene red carbonyl groups was discussed in detail previously [12].

At first it seems counterintuitive that the oxygen content rises from ~ 10 to $\sim 25\%$ atomic with increasing IrRu loading (Fig. 2) and yet most, about 75%, of Pt, Ir, and Ru content is present in metallic form for all the loadings. However, a careful stoichiometry inspection shows that for each loading the available oxygen nicely correlates to the atomic concentrations of the resolved reacted forms of Ir, Ru, C, and Pt (Table 1). In order to fully assess the interfacial stoichiometry, the atomic concentrations of C–O functional groups, which was only about 1–2% for all the catalyst loadings, were also taken into account.

For the IrRu loading of $1 \mu\text{g cm}^{-2}$, predominantly Pt resides on the surface (Fig. 2), which means that most of the present $\sim 10\%$ atomic of oxygen is coming from the Pt–O bonds. The calculated atomic concentration of the reacted Pt in Table 1 is ~ 15 – 20%

Table 1
Atomic concentrations of resolved metallic and reacted Ir, Ru and Pt derived from XPS spectra.

OER Catalyst loading, $\mu\text{g cm}^{-2}$	Ir metallic % at	Ir reacted % at	Ru metallic % at	Ru reacted % at	Pt metallic % at	Pt reacted % at
1	4.0	0.9	0.3	0.1	44.7	17.4
2	8.5	2.1	0.5	0.2	37.7	15.5
3	20.5	5.5	0.8	0.3	24.4	9.8
10	29.4	8.2	0.6	0.2	12.7	5.4

(within the quantification accuracy of the XPS method). Thus, the stoichiometry of the formed platinum oxide is most probably PtO or Pt₂O. The existence of Pt–O–C bonds is also a possibility. The derived stoichiometry is in agreement with the BE shift of the reacted platinum peak, which indicates that the reacted platinum is mostly present in the form of Pt suboxides or Pt(II) oxides (Fig. 4c,d). Also, the contribution of the oxide oxygen peak is lower for the low IrRu loadings (Fig. 5c,d). For the IrRu loading of 10 $\mu\text{g cm}^{-2}$, there is two times more Ir than Pt on the surface (Fig. 2). The detected oxygen content of about 20% atomic is shared between Ir and Pt, but it is primarily associated with the Ir–O bonds. Considering that the calculated atomic concentration of the reacted Ir is about 10%, and that the shift of the resolved reacted Ir 4f peak corresponds to the Ir(III) and Ir(IV) oxide forms, which require more oxygen, the observed increase in the oxygen content can be explained.

3.2. Electrochemical evaluation

We have previously shown that reductions in electrochemically active surface area (ECSA) and fuel cell performance losses were directly related to the ability of the OER catalyst to maintain the cathode potential well below the 1.6 V limit [10]. A summary of the ECSA data is presented in Fig. 6. The beginning-of-life (BOL) and end-of-life (EOL) ECSA is plotted in terms of percent difference relative to bare Pt-NSTF. The net difference between EOL and BOL performance is plotted as well.

Prior to testing, the presence of the OER catalyst on the NSTF whisker surfaces had a small effect on the ECSA of the Pt ORR catalyst, as shown in Fig. 6, arising from the blockage of Pt surface sites by the IrRu overlayer. Following testing, the ECSA measurements showed a significant trend with OER loading. While the ECSA for bare Pt dropped by nearly 50%, the change in ECSA for the OER samples was significantly lower and improved with OER catalyst loading. An even greater improvement over bare Pt was observed based on the net EOL-BOL change, where the highest OER loading (10 $\mu\text{g cm}^{-2}$) showed less than 10% change in ECSA over the life of the test.

3.3. Changes in whisker morphology

For conventional Pt/C catalysts, a decrease in catalyst ECSA has been linked to microstructural changes due to Pt dissolution, particle coalescence/agglomeration, and particle encapsulation [16–18]. However, as noted in ref. [19], the film-like structure of the Pt NSTF contains fewer sharp edge sites from which rapid dissolution might occur. Since there are no small particles to coalesce

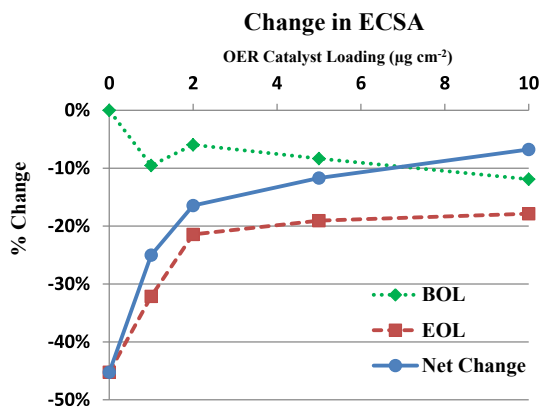


Fig. 6. Beginning-of-life, end-of-life, and net percent change in ECSA for different OER catalyst loadings in MEAs submitted to SU/SD test conditions [10]. The BOL Pt-NSTF with no OER catalyst was used as the reference value.

and coarsen, the authors associated the change in ECSA after potential cycling to a general smoothing of the NSTF whisker surface via dissolution and redeposition of Pt. Such smoothing was also observed in the present work following the SU/SD test, and, as summarized in Fig. 7, the degree of dissolution-driven smoothing is directly related to the OER loading. The highly structured surface of the BOL whisker walls (arrowed and outlined) is still observed to some extent in the EOL whiskers with 5 and 10 $\mu\text{g cm}^{-2}$ OER catalyst loadings. The whisker surface becomes increasingly smooth as OER loading is reduced. As outlined, the structured surface is all but lost in the EOL Pt-only sample.

In an effort to quantify the degree of NSTF surface smoothing, a simple script was written for the Gatan DigitalMicrograph software suite (used for image analysis of TEM/STEM images) to calculate the root mean squared roughness (R_q) of the whisker surfaces (see Fig. 8a,b). The average value of R_q was determined for each OER loading, summarized in Table 2, and confirms the correlation between OER catalyst loading, ECSA losses, and smoothing of the whisker surfaces. While smoothing can account for some of the surface area change, it does not take into account the surface area losses resulting from Pt dissolution and migration into the membrane, which will result in additional thinning of the nano-structured Pt catalyst film. Thus, the average catalyst layer thickness was measured (given in Table 2), which also correlates directly with OER catalyst loading. The smoothing of the whisker surfaces indicates the loss of surface area results from the combination of the geometric surface change and the permanent loss of Pt catalyst to the membrane.

It should be noted that in alloyed NSTF catalyst systems, such as PtNi, smoothing of the whisker surfaces can, in fact, result in a pronounced increase in catalyst activity due to the formation of a Pt-skin structure [20]. Further, as Pt(110) planes have been shown to have the highest ORR activity [21], the formation of a catalyst film-like structure with this preferred surface orientation would lead to an enhancement in activity [22]. Inspection of the whisker surfaces of the Pt NSTF sample (Fig. 9) shows that smoothing does not result in a single crystal thin film, but instead a polycrystalline film with a crystal size on the order of 5–10 nm. No strongly preferred surface orientation was observed, which is an aspect that requires a more detailed investigation.

Closer inspection of the OER-coated whisker surfaces after SU/SD testing showed the presence of small nanoparticles not previously observed in the BOL samples. The HAADF-STEM images presented in Fig. 10 show these particles, both on the surface of the whisker and in the adjacent membrane. Spectroscopic analysis indicated the particles were a mixture of Ir and Pt, with Ir being the primary component. The presence of similar particles within the membrane will be discussed in Section 3.4.

3.4. Changes in whisker composition

Since Ru, Ir, and Pt were not readily discernable in the high-resolution TEM or STEM images, EDS elemental mapping was used to distinguish the layer compositions. Fig. 11 presents EDS maps for Ir and Pt at 2, 5, and 10 $\mu\text{g cm}^{-2}$ OER loadings, both before (Fig. 11a–d) and after (Fig. 11e–h) testing. Due to an overlap with the intense Pt-L peak, it was difficult to reliably map or quantify Ir at the lowest loading (1 $\mu\text{g cm}^{-2}$). Ru was detectable at the highest loading (10 $\mu\text{g cm}^{-2}$), but was difficult to detect at lower loadings, especially due to overlap of the Ru-L peak with higher order Pt-M peaks in the EDS spectra. Thus, the EDS analysis mainly focused on Ir and Pt for the three highest OER loadings.

It appears from the elemental maps in Fig. 11a,b that Ir covers a significant portion of the Pt surface at the two highest loadings. However, the degree of coverage is likely somewhat exaggerated by

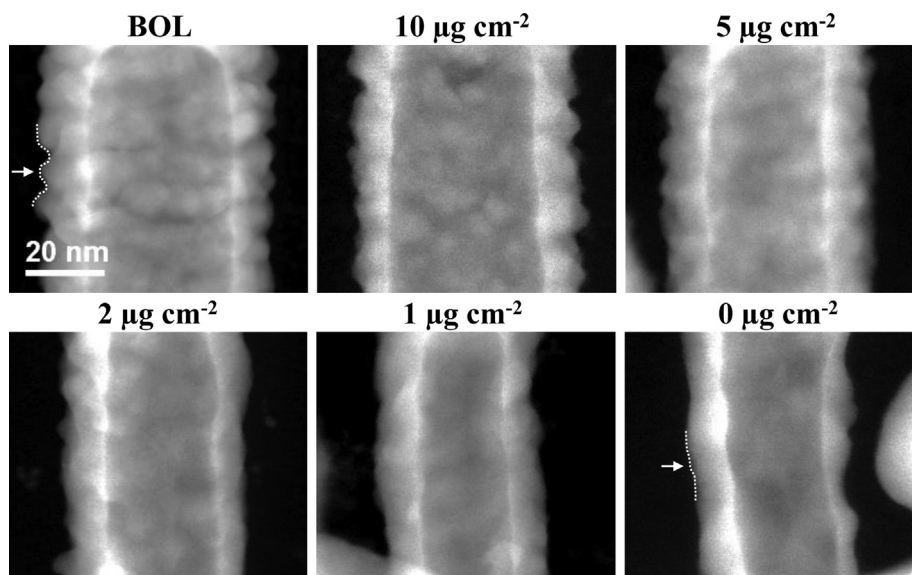


Fig. 7. HAADF-STEM images of individual whiskers after SU/SD testing for each OER catalyst loading, with a BOL image provided for reference. The degree of smoothing of the whisker surfaces, an indicator of Pt dissolution, is inversely related to the OER catalyst loading. Compare the arrow/outline regions in BOL and EOL 0 $\mu\text{g cm}^{-2}$ loading (pure-Pt).

the overlapping Pt grains, limited spatial resolution of EDS (1–2 nm), and the smoothing/averaging routines used to generate the elemental maps. It was shown in Fig. 6 that the catalyst loading does impact the initial ECSA. At the lower loading ($2 \mu\text{g cm}^{-2}$), it is clear that the Ir layer is discontinuous, with limited surface coverage especially along the NSTF side-walls, thus leaving a majority of Pt sites available for the ORR.

Of key interest in this study was determining the retention of the OER catalyst on the NSTF surfaces after SU/SD testing. The EDS maps acquired from the whisker surfaces after testing, shown in Fig. 11e–g, indicate that significant Ir is retained on the NSTF surfaces. Further, by comparing the EDS line profiles across the whisker cross-sections, shown in Fig. 11d,h for the BOL and EOL cathodes, respectively, it is clear that the Ir does not alloy with the underlying Pt catalyst or is coated by Pt during the dissolution and redeposition process. Instead, the Ir remains relatively stable on the surface of the Pt catalyst and continues to be available for the OER.

The overall change in the Ir to Pt ratio was evaluated by quantifying the Ir and Pt wt.% in the BOL and EOL cathodes. This was done by acquiring EDS spectra from 15 to 20 individual whiskers for each of the BOL and EOL samples at each OER loading. Since it was

discovered that Ir:Pt at the whisker tips was, on average, 25% higher than on the whisker side-walls, the tip regions were excluded during EDS data collection. The results from this analysis for the 2, 5, and $10 \mu\text{g cm}^{-2}$ OER catalyst loadings are shown inset in Fig. 11a–c for each loading for the BOL cathode and Fig. 11e–g for each loading for the EOL cathode (note green text inset). Overall, the Ir wt.% remained relatively constant after SU/SD testing, with a slight increase for the $10 \mu\text{g cm}^{-2}$ loading and slight decrease for the $2 \mu\text{g cm}^{-2}$ loading, which suggests that Pt and Ir dissolution proceeded at approximately the same rate, and that Ir is indeed stable under SU/SD conditions. Although it was not possible to quantify the amount of OER catalyst lost, previously reported OER performance values [10] indicate that sufficient OER catalyst losses occurred to impact performance at the $2 \mu\text{g cm}^{-2}$ loading. However, as shown by the EDS maps and quantification, sufficient catalyst remained on the whisker surface to provide an OER current well above that of the pure Pt NSTF baseline.

3.5. Migration of catalysts throughout the MEA

The dissolution and subsequent transport of the Pt catalyst atoms through the fuel cell MEA was observed at multiple length scales, sub-nm to μm . Fig. 12a and c compare SEM cross-section MEA images of the EOL cathodes of SU/SD tested MEAs for a pure Pt-NSTF and for a Pt-NSTF with a $2 \mu\text{g cm}^{-2}$ OER loading, respectively. In the pure Pt-NSTF cathode, large Pt particles had formed a distinct ‘band’ in the membrane $\sim 20 \mu\text{m}$ from the cathode. In the case of the OER-decorated Pt-NSTF, the Pt particle band was typically confined to within $5 \mu\text{m}$ of the cathode. The Pt particles were far fewer in number, but also larger than those observed in the Pt-only NSTF sample. The loading and dispersion of Pt within the membrane has been shown to impact the severity of membrane degradation through radical formation [23]. Further research would be needed to understand the impact of the OER catalyst on Pt diffusion and membrane degradation.

On a finer length scale, HAADF-STEM images of cross-sectioned MEAs are shown in Fig. 12b and d for the EOL cathodes of SU/SD tested MEAs for a pure Pt-NSTF and for a Pt-NSTF with a $2 \mu\text{g cm}^{-2}$ OER loading, respectively, of the membrane region between the

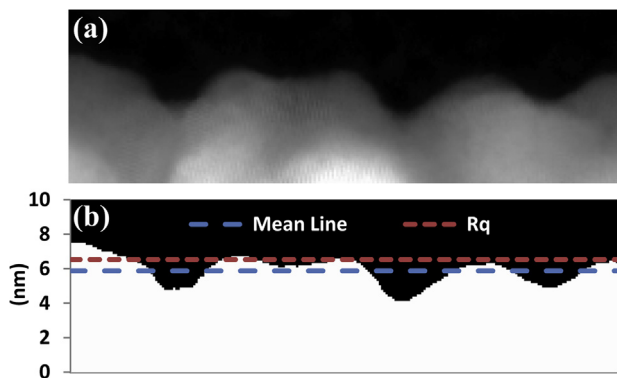


Fig. 8. (a) HAADF-STEM images of whisker surface with (b) two-tone image showing the mean and root-mean-squared roughness (R_q) lines. The R_q value was used for quantifying the degree of surface smoothing.

Table 2
Electrochemically active surface area (ECSA), mean square roughness (R_q), and final thickness of Pt layer following testing (EOL) for different OER catalyst loadings. The beginning of life (BOL) data for the $10 \mu\text{g cm}^{-2}$ loading is included for reference.

	OER loading ($\mu\text{g cm}^{-2}$)					
	0	1	2	5	10	BOL 10
EOL ECSA ($\text{m}^2 \text{m}^{-2}$)	4.6 ± 0.7	5.7 ± 0.6	6.6 ± 0.3	6.8 ± 0.7	6.9 ± 0.4	7.4 ± 0.9
R_q (nm)	0.37 ± 0.09	0.51 ± 0.14	0.64 ± 0.13	0.72 ± 0.07	0.79 ± 0.22	0.93 ± 0.15
Pt thick. (nm)	7.9 ± 1.2	9.0 ± 1.3	9.2 ± 0.9	9.3 ± 0.9	9.7 ± 0.8	11.9 ± 1.7

cathode and the Pt band, which reveals the presence of fine-scale particles in the membrane only for the OER catalyst-containing MEAs. The largest particles were found nearest the membrane/cathode interface and tended to agglomerate. The particles were extremely sensitive to the electron beam during imaging and EDS analysis, but were found to contain both Pt and Ir. As shown in Fig. 13a, the size of the particles decreased with distance into the membrane, with a notable increase in the crystallinity of the nanoparticles. The Pt concentration was highest within the particles near the NSTF, at roughly 25 wt.%, but the Pt content within the particles decreased rapidly with distance into the membrane, in parallel with the decrease in particle size and increase in nanoparticle crystallinity, indicating that the smallest crystalline particles were likely pure Ir. The IrPt particles were limited to the region between the cathode and the Pt band. Increased crystallinity is likely related to a reduction in the oxide content of the particles, but this was difficult to determine due to the oxygen background from the membrane.

For conventional Pt/C electrodes, the mechanisms contributing to Pt dissolution and subsequent formation of the Pt band in the membrane have been studied extensively [16,24,25]. Dissolved Pt^{2+} can either be recaptured within the electrode, leading to Pt particle coarsening [26], or can migrate into the membrane, where it is reduced by H_2 crossing over from the anode forming a distinct band of relatively large Pt particles, the location of which is determined

by the partial pressures of H_2 and O_2 at the anode and cathode, respectively [27–29]. The region between the cathode and Pt band is often reported to be devoid of Pt in conventional electrodes, similar to the behavior observed for the Pt-only NSTF sample. Thus, the presence of Ir must play an integral role in the formation of the agglomerates.

Recent work on Nafion-stabilized Ir and Pt nanoparticles synthesized by alcohol reduction found that Ir tends to form very small, highly dispersed nanoparticles, while Pt nanoparticles tend to agglomerate into larger clusters [30,31]. In the present work, Ir appears to readily stabilize within the membrane near the NSTF cathode. The Ir nanoparticles may provide temporary nucleation sites for dissolved Pt, which in turn drives the formation of agglomerated nanoparticles. The Pt can then re-dissolve and migrate deeper into the membrane, where it forms the larger and more stable particles within the Pt band [32].

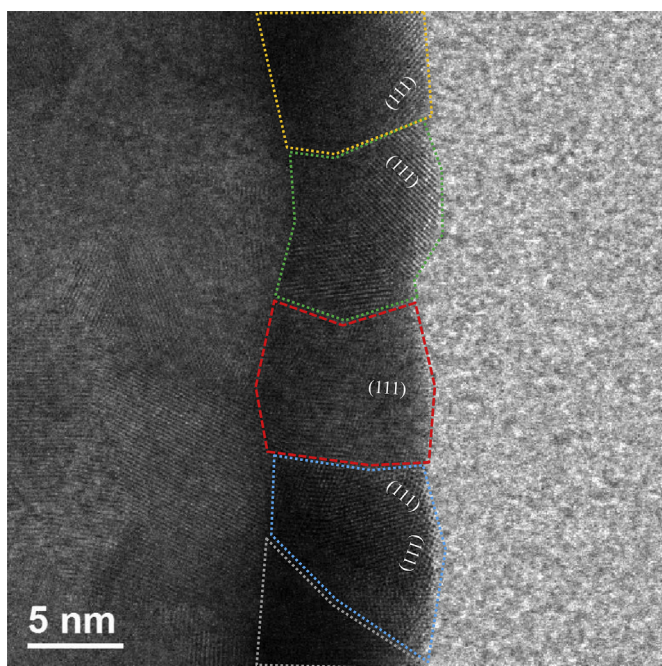


Fig. 9. Bright-field STEM image of the surface of a pure Pt-NSTF whisker following SU/SD cycling. The smoothed surface film is comprised of individual Pt grains (5–10 nm), which are outlined in the image. The (111) lattice planes are labeled in each grain, show no clear preferred direction relative to the whisker surface.

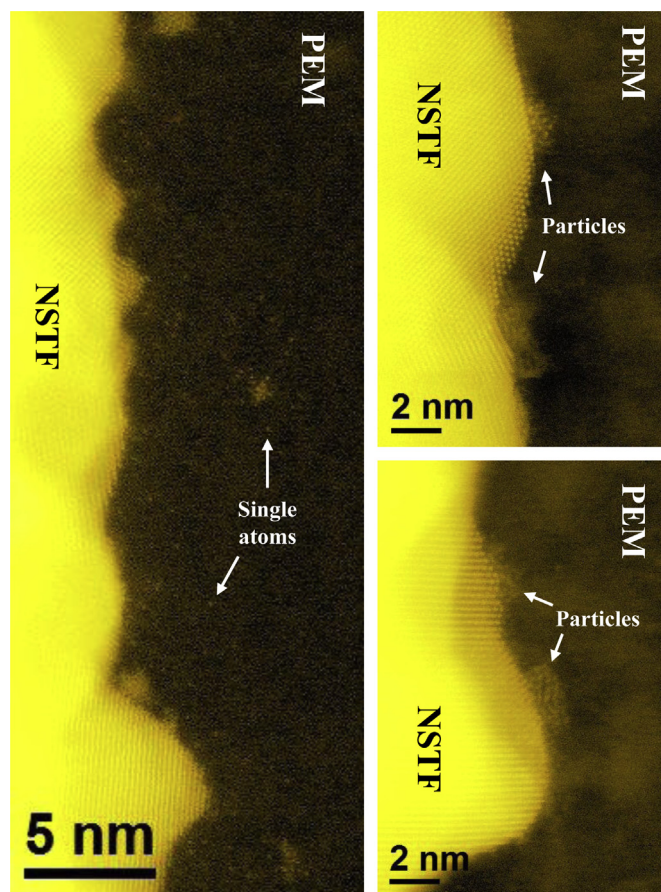


Fig. 10. HAADF-STEM images of whisker surfaces following SU/SD cycling for an OER catalyst loading of $5 \mu\text{g cm}^{-2}$. False color was used to highlight the presence of IrPt nanoparticles on the surfaces and within the membranes. Arrows point to individual atoms within the membrane. (For interpretation of the references to color in this figure legend, the reader is referred to the web version of this article.)

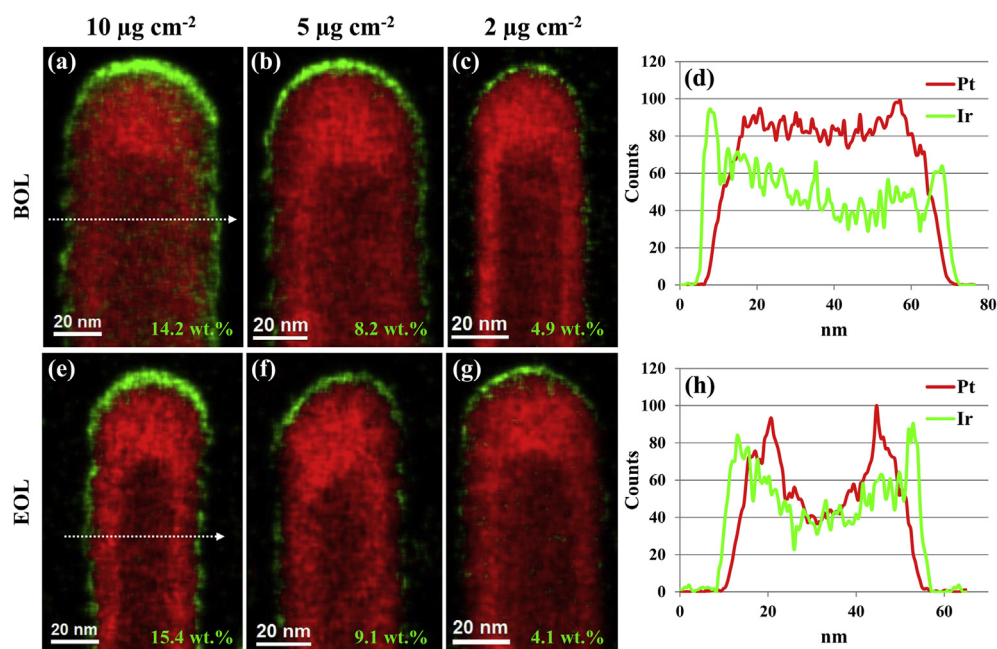


Fig. 11. EDS maps (Ir: green, Pt: red) for (a–c) BOL and (e–g) EOL whiskers for different OER catalyst loadings showing retention of the Ir catalyst following SU/SD tests. EDS line scans in (d,h) correspond to lines in (a,e), and show that no alloying occurs between the Ir and Pt during SU/SD, nor does dissolved Pt redeposit over the OER catalyst. (For interpretation of the references to color in this figure legend, the reader is referred to the web version of this article.)

Thus, the addition of the OER catalyst not only had the intended effect of reducing catalyst support corrosion and ORR catalyst degradation by limiting peak cathode voltages, but also had an inadvertent impact by reducing Pt loss through dissolution and migration into membrane. As discussed, the potential impact of reducing Pt migration on fuel cell performance is not yet clear,

especially since the effect of Pt band formation on MEA durability in general remains under investigation [33].

It should be noted that no Ru was found in the membrane. However, inspection of the MPL adjacent to the cathode by HAADF-STEM imaging revealed dispersed nanoparticles (Fig. 13e), which were identified as Ru via EDS analysis. The instability of Ru in the

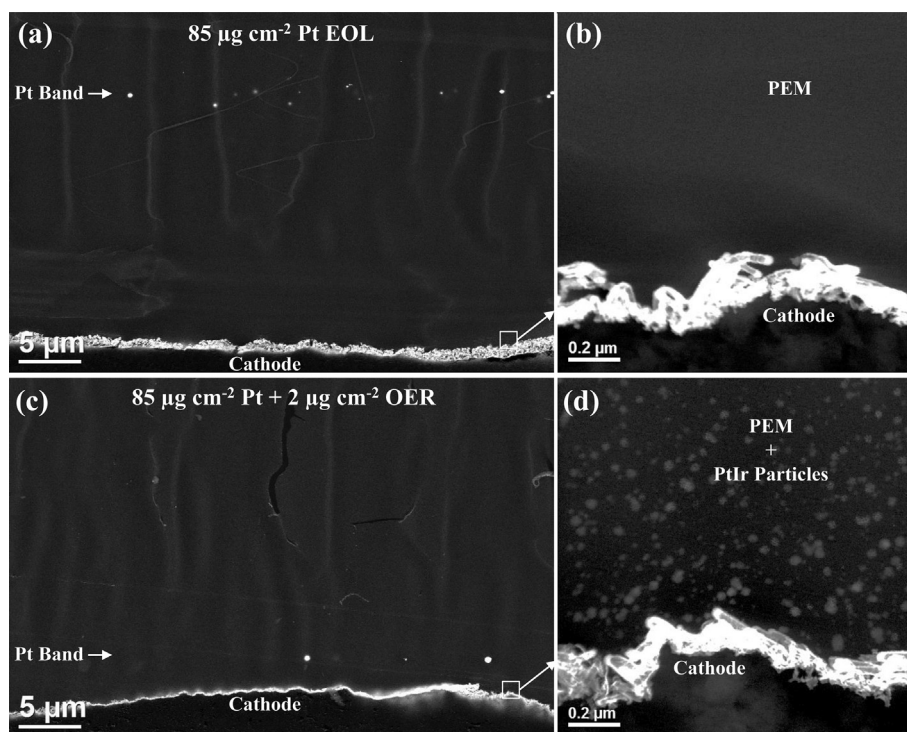


Fig. 12. SEM (a,c) and STEM images (b,d) of MEAs with and without an OER catalyst on the cathode, respectively. The OER catalyst affects both the location and density of the Pt band. Nanoparticles were also found between the cathode and Pt band in the OER-containing MEAs.

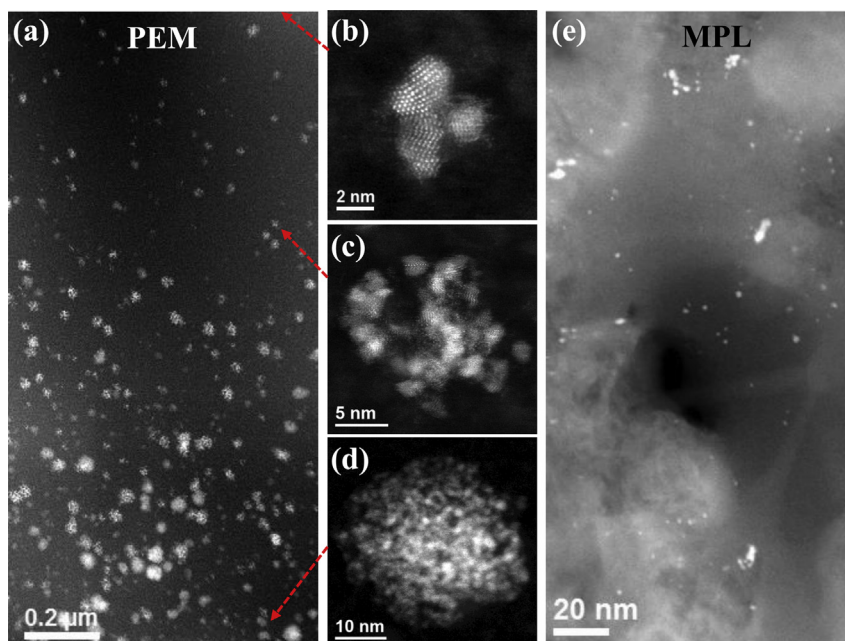


Fig. 13. HAADF-STEM images of (a–d) IrPt agglomerates in the membrane and (e) Ru particles in the MPL. The cathode is located at the bottom of (a), with (b) representing Ir nanoparticles closer to the Pt band and (d) large IrPt nanoparticle agglomerate near the NSTF cathode.

fuel cell environment at high positive potentials is well documented in the literature, especially for the case of PtRu/C anodes used in direct methanol fuel cells, where Ru dissolution and crossover to the cathode is problematic [34]. Another study showed that Ru did not plate the cathode surface, but instead migrated to the cathode/GDL interface, where Ru ions were thought to be electro-deposited as RuO_x [35]. A similar behavior is observed in this case, albeit careful EELS analysis of Ru in the MPL layer found no evidences of oxygen associated with the Ru particles.

4. Summary

The influence of IrRu OER catalysts on the stability of Pt-NSTF electrodes under SU/SD conditions has been investigated for different OER loadings. The presence of the OER catalyst greatly improved the durability of the Pt catalyst by enhancing the electrolysis of water at lower potentials than that experienced by pure Pt-NSTF electrodes. XPS and STEM characterization of the as-grown catalyst showed that Ir is primarily in a metallic state and tends to grow epitaxially on the Pt surfaces. Further evidence was presented which suggests that Ru prefers to deposit on exposed perylene-red support sites.

Following SU/SD testing, it was demonstrated that the presence of the OER catalyst limited Pt dissolution, as evidenced at the electrochemical level by the preservation of the catalyst ECSA, and at the microstructural level by limited smoothing of the NSTF surfaces and reduced Pt band formation in the membrane. The OER catalyst also limited the migration of dissolved Pt, as evidenced by the increased proximity of the Pt band to the cathode and the presence of PtIr nanoparticles between the cathode and Pt band, compared to similar results obtained for the Pt-only-NSTF. The Ir to Pt ratio of individual whiskers remained relatively constant following SU/SD, and alloying of Ir and Pt on the whiskers was not observed. Ruthenium, the least stable of the three catalyst components, was discovered in the MPL as nanoparticles. Crossover of the OER/ORR catalysts to the anode was not observed under any SU/SD test conditions.

The electrochemical and structural measurements in this and previous work indicate that an OER catalyst loading of $2 \mu\text{g cm}^{-2}$ provides the optimal balance for NSTF catalysts between performance, durability, and cost. Ongoing investigations, combined with additional characterization methods, aim to understand and improve on the remarkable activity and durability of minute loadings of the $\text{Ir}_{0.9}\text{Ru}_{0.1}$ catalyst towards the OER in MEAs exposed to transient conditions. These catalysts are also under investigation as additives to the anode for mitigating the impact of cell reversal events.

Acknowledgments

This work was supported by the Fuel Cell Technologies Office, Office of Energy Efficiency and Renewable Energy, U.S. Department of Energy under Award Number DE-EE0000456 and through a user project supported by ORNL's Center for Nanophase Materials Sciences (CNMS), which is sponsored by the Scientific User Facilities Division, Office of Basic Energy Sciences, U.S. Department of Energy.

References

- [1] F.T. Wagner, B. Lakshmanan, M.F. Mathias, J. Phys. Chem. Lett. 1 (2010) 2204–2219.
- [2] C.A. Reiser, L. Bregoli, T.W. Patterson, J.S. Yi, J.D. Yang, M.L. Perry, T.D. Jarvi, Electrochem. Sol. St. 8 (2005) A273–A276.
- [3] Y. Yu, H. Li, H. Wang, X.Z. Yuan, G. Wang, M. Pan, J. Power Sources 205 (2012) 10–23.
- [4] J.E. Owejan, P.T. Yu, R. Makharia, ECS Trans. 11 (2007) 1049–1057.
- [5] R.T. Atanasoski, L.L. Atanasoska, D.A. Cullen, G.M. Haugen, K.L. More, G.D. Vernstrom, Electrocatalysis 3 (2012) 284–297.
- [6] S. Trasatti, Electrochim. Acta 29 (1984) 1503–1512.
- [7] R. Kötz, S. Stucki, Electrochim. Acta 3 (1986) 1311–1316.
- [8] M.K. Debe, ECS Trans. 45 (2012) 47–68.
- [9] M.K. Debe, in: W. Vielstich, H.A. Gasteiger, A. Lamm (Eds.), Handbook of Fuel Cells – Fundamentals, Technology, and Applications, Wiley, New York, 2003, p. 576.
- [10] R.T. Atanasoski, D.A. Cullen, G.D. Vernstrom, G.M. Haugen, L.L. Atanasoska, ECS Electrochem. Lett. 2 (2013) F25–F28.
- [11] D.A. Blom, J.R. Dunlap, T.A. Nolan, L.F. Allard, J. Electrochem. Soc. 150 (2003) A414–A418.
- [12] (a) L.L. Atanasoska, D.A. Cullen, A.E. Hester, R.T. Atanasoski, ECS Trans. 50 (2013) 19–33;

- (b) L.L. Atanasoska, D.A. Cullen, R.T. Atanasoski, J. Serb. Chem. Soc. 78 (2013) 1993–2005.
- [13] L. Atanasoska, R. Atanasoski, S. Trasatti, *Vacuum* 40 (1990) 91–94.
- [14] (a) S. Zafeiratos, G. Papakonstantinou, M.M. Jacksic, S.G. Neophytides, J. Catal. 232 (2005) 127–136;
(b) M. Peuckert, H.P. Bonzel, *Surf. Sci.* 145 (1984) 239–259;
(c) V.K. Kaushik, Z. Phys. Chem. 173 (1991) 105–113.
- [15] L. Atanasoska, P. Gupta, C. Deng, R. Warner, S. Larsen, J. Thompson, *ECS Trans.* 16 (2009) 37–48.
- [16] P.J. Ferreira, G.J. la O', Y. Shao-Horn, D. Morgan, R. Makharia, S. Kocha, H.A. Gasteiger, *J. Electrochem. Soc.* 152 (2005) A2256–A2271.
- [17] F.A. de Bruijn, V.A.T. Dam, G.J.M. Janssen, *Fuel Cells* 8 (2008) 3–22.
- [18] K.J.J. Mayrhofer, S.J. Ashton, J.C. Meier, G.K.H. Wiberg, M. Hanzlik, M. Arenz, *J. Power Sources* 185 (2008) 734–739.
- [19] A. Kongkanand, Z. Liu, I. Dutta, F.T. Wagner, *J. Electrochem. Soc.* 158 (2011) B1286–B1291.
- [20] D.F. van der Vliet, C. Wang, D. Tripkovic, D. Strmcnik, X.F. Zhang, M.K. Debe, R.T. Atanasoski, N.M. Markovic, V.R. Stamenkovic, *Nat. Mater.* 11 (2012) 1051–1058.
- [21] V.R. Stamenkovic, B.S. Mun, K.J.J. Mayrhofer, P.N. Ross, N.M. Markovic, *J. Am. Chem. Soc.* 128 (2006) 8813–8819.
- [22] W.J. Khudhayer, N.N. Kariuki, X. Wang, D.J. Myers, A.U. Shaikh, T. Karbacak, *J. Electrochem. Soc.* 128 (2011) B1029–B1041.
- [23] M.P. Rodgers, B.P. Pearman, L.J. Bonville, D.A. Cullen, N. Mohajeri, D.K. Slattery, *J. Electrochem. Soc.* 160 (2013) F1123–F1128.
- [24] R.M. Darling, J.P. Meyers, *J. Electrochem. Soc.* 150 (2003) A1523–A1527.
- [25] S.G. Rinaldo, J. Stumper, M. Eikerling, *J. Phys. Chem. C* 114 (2010) 5773–5785.
- [26] A. Virkar, Y. Zhou, *J. Electrochem. Soc.* 154 (2007) B540–B547.
- [27] K. Yasusda, A. Taniguchi, T. Akita, T. Ioroi, Z. Siroma, *Phys. Chem. Chem. Phys.* 8 (2006) 746–752.
- [28] W. Bi, G.E. Gray, T.F. Fuller, *Electrochem. Sol. St.* 10 (2007) B101–B104.
- [29] P.J. Ferreira, Y. Shao-Horn, *Electrochem. Sol. St.* 10 (2007) B60–B63.
- [30] Y. Zhang, H. Zhang, Y. Zhang, Y. Ma, H. Zhong, H. Ma, *Chem. Commun.* 43 (2009) 6589–6591.
- [31] Z. Liu, Z.Q. Tian, S.P. Jiang, *Electrochim. Acta* 52 (2006) 1213–1220.
- [32] S.F. Burlatsky, M. Gummalla, V.V. Atrazhev, D.V. Dmitriev, N.Y. Kuzminyh, N.S. Erikhman, *J. Electrochem. Soc.* 158 (2011) B322–B330.
- [33] B.P. Pearman, N. Mohajeri, R.P. Brooker, M.P. Rodgers, D.K. Slattery, M.D. Hampton, D.A. Cullen, S. Seal, *J. Power Sources* 225 (2013) 75–83.
- [34] E. Antolini, *J. Solid State Electrochem.* 15 (2011) 455–472.
- [35] Y. Chung, C. Pak, G.-S. Park, W.S. Jeon, J.-R. Kim, Y. Lee, H. Chang, D. Seung, *J. Phys. Chem. C* 112 (2008) 313–318.